International Journal of Extreme Manufacturing

Printability disparities in heterogeneous material combinations via laser directed energy deposition: a comparative study

OPEN ACCESS
IOP Publishing | IMMT
International Journal of Extreme Manufacturing
Int. J. Extrem. Manuf. **6** (2024) 025001 (17pp)
https://doi.org/10.1088/2631-7990/ad172f

Printability disparities in heterogeneous material combinations via laser directed energy deposition: a comparative study

Jinsheng Ning[1,6], Lida Zhu[1,6,*], Shuhao Wang[2], Zhichao Yang[1], Peihua Xu[1], Pengsheng Xue[3], Hao Lu[1], Miao Yu[1], Yunhang Zhao[1], Jiachen Li[4], Susmita Bose[5] and Amit Bandyopadhyay[5,*]

[1] School of Mechanical Engineering and Automation, Northeastern University, Shenyang 110819, People's Republic of China
[2] School of Machinery and Automation, Wuhan University of Science and Technology, Wuhan 430081, People's Republic of China
[3] School of Mechanical Engineering, Xi'an University of Science and Technology, Xi'an 710054, People's Republic of China
[4] Beijing Institute of Space Launch Technology, Beijing 100076, People's Republic of China
[5] W. M. Keck Biomedical Materials Research Lab, School of Mechanical and Materials Engineering, Washington State University, Pullman, WA 99164, United States of America

E-mail: neulidazhu@163.com and amitband@wsu.edu

Received 30 May 2023, revised 10 September 2023
Accepted for publication 19 December 2023
Published 4 January 2024

Abstract

Additive manufacturing provides achievability for the fabrication of bimetallic and multi-material structures; however, the material compatibility and bondability directly affect the parts' formability and final quality. It is essential to understand the underlying printability of different material combinations based on an adapted process. Here, the printability disparities of two common and attractive material combinations (nickel- and iron-based alloys) are evaluated at the macro and micro levels via laser directed energy deposition (DED). The deposition processes were captured using *in situ* high-speed imaging, and the dissimilarities in melt pool features and track morphology were quantitatively investigated within specific process windows. Moreover, the microstructure diversity of the tracks and blocks processed with varied material pairs was comparatively elaborated and, complemented with the informative multi-physics modeling, the presented non-uniformity in mechanical properties (microhardness) among the heterogeneous material pairs was rationalized. The differences in melt flow induced by the unlike thermophysical properties of the material pairs and the resulting element intermixing and localized re-alloying during solidification dominate the presented dissimilarity in printability among the material combinations. This work provides an in-depth understanding of the phenomenological differences in the deposition of dissimilar materials and aims to guide more reliable DED forming of bimetallic parts.

[6] These authors contributed equally to this work.
[*] Authors to whom any correspondence should be addressed.

2631-7990/24/025001+17$33.00

Supplementary material for this article is available online

Keywords: directed energy deposition, printability, microstructure, microhardness, bimetallic parts

Abbreviation

AM	Additive manufacturing
CFD	Computational fluid dynamics
DED	Directed energy deposition
EDS	Energy dispersive spectrometer
EBSD	Electron backscatter diffraction
HAZ	Heat-affected zone
IPFs	Inverse pole figures
MUD	Multiples of uniform distribution
EZ	Elevation zone
PZ	Penetration zone
BZ	Bonding zone
ZOIs	Zones of interest
D-S boundary	Deposited layer-substrate boundary
M-S junction	Melt pool-substrate junction
SEM	Scanning electron microscope
SS	Stainless steel
Ni_{eq}	Equivalent Ni element
P_{cm}	Critical weldability
ED	Energy density
P	Laser power (W)
S	Scanning speed ($mm \cdot min^{-1}$)
F	Powder feed rate ($g \cdot min^{-1}$)
d	Depth of melt pool (mm)
d_0	Laser beam waist diameter −3 mm
w	Width of melt pool (mm)
$d\ w^{-1}$	Aspect ratio of the melt pool
Nickel/iron	Ni-based material printed onto Fe-based material
Iron/nickel	Fe-based material printed onto Ni-based material

1. Introduction

Metals are indispensable in the real world, and various metallic components have long served in many critical industries, such as automotive, aerospace, and healthcare [1–4]. Nature-inspired [5] or application-oriented [6] multi-material integrated parts are becoming increasingly popular [7, 8]. Both simple bimetallic systems and relatively complex multi-material hierarchical structures have potential using prospects due to their unique physical or mechanical properties that can fulfill the individualized functions at specific sites [9–12]. Unlike most single metallic materials that are easily machinable, conventional processing (e.g. fusion welding, diffusion bonding) may be challenging to build these parts integrated with multiple materials with uniform or gradient interfaces.

DED, a popular metal AM approach, provides a viable solution for integrating multiple materials [13, 14]. This attractive technique is relatively efficient with a high degree of design freedom, which can meet the demand for diversified and customized manufacturing of metallic parts [15, 16]. Considerable theoretical developments and experimental research have demonstrated the feasibility of DED for multi-material forming. The most basic means for producing compositionally graded alloys are directly depositing one material onto another, namely the bimetallic structures [17, 18]. Onuike *et al* [19] processed Inconel 718 and GRCop-84 copper alloy bimetallic structures using laser engineered net shaping and adopted the same manufacturing approach for crack-free bimetallic structures of Inconel 718 and Ti6Al4V. Sahasrabudhe *et al* [20] successfully deposited Ti64 onto the SS410 substrate and the compositionally graded bimetallic structures. Li *et al* [21] fabricated bimetallic parts that consist of nickel–aluminum–bronze and 15–5 PH via DED. Zhang *et al* [22] used the DED process to obtain a well-bonded copper and SS 316L hybrid part by introducing a nickel-based alloy between the target materials. Even for refractory metals, the manufacturability of their dissimilar mixture (e.g. Ti and Zr, Nb) via DED has been computationally proven with a high-fidelity model conducted by Shinjo and Panwisawas [23].

Multi-material parts with the metallurgical transition of the linear gradient can be achieved using DED [11, 24]. For instance, Lin *et al* [25] used laser rapid forming to successfully produce a graded material multilayer part with a linear compositional gradient from 100% SS316L to 100% Rene88DT superalloy. Melzer *et al* [26, 27] printed functionally graded materials containing Inconel 718 and SS316L using a DED system and performed detailed metallographic and fractographic investigations. Zhang *et al* [28] fabricated Ti-Al_2O_3 compositionally graded components using a laser-based deposition method for the first time. This work demonstrated the single-step multi-material metal-ceramic composite manufacturing feasibility of maintaining the part dimensions and compositional variations. Ben-Artzy *et al* [29] used DED to print a part coupled with SS316L and C300 maraging steel, incorporating a spatially varying composition between the two primary materials (13 discrete composition layers) to achieve a smooth transition in properties and microstructure. Regarding the practicability of DED in building more complicated material distributions, Tan *et al* [30] have attempted to successfully build a configurable voxelized architecture based on two classes of stainless-steel materials-martensitic grade 300 maraging steel and SS316 L, and they demonstrated that the two materials intertwined together using DED exhibited better mechanical properties.

Based on the compatibility of multiple materials forming by complex printing, the further points are to achieve and optimize the use functionality and mechanical performance.

Most existing publications have focused on the macroscopic mechanical properties of the printed multi-material parts, such as the interfacial characteristics [31, 32], tensile or compressive behavior [33], and fracture toughness [27]; meanwhile, at the microscopic level, issues such as metallographic organization and element precession have also been covered [34–36]. Attempts are being made to clarify the scientific aspects of DED forming—'material-process (parameter)-property.' Regarding bimetallic or multi-material DED fabrication, the key issues can be traced to the complex deposition processes [37], which include the forming process uncertainties (i.e. process and property differences due to the heterogeneous and non-compatible materials) and the instabilities at the melt pool due to different material combinations. Unfortunately, scientific results of the fundamental forming behaviors of DED forming with multiple materials are still scarce.

Ni-based alloys and steels have been frequently selected for investigations in bimetallic research. Typically, the Inconel (a class of Ni-based alloys) is extensively used in aero and space industries because of excellent high-temperature mechanical properties, along with favorable oxidation and corrosion resistance [38, 39]; SSs are more economical by comparison and used extensively in numerous applications due to their excellent corrosion resistance along with favorable mechanical properties [40]. Although IN718 (or IN625) and SS316L share an identical crystal structure of face-centered cubic (FCC) and the difference in the coefficient of thermal expansion between them is relatively minor, the interface between these dissimilar materials is the weakest place of such bimetallic structures due to intermetallic phase formation [26]. Given their widespread popularity and attention, the two types of nickel-based alloys (i.e. IN718, IN625) and iron-based SS316L are used in this study.

To further understand and explore the role of heterogeneous material combination in formability and printability, this work specifically examines the process of the single-track forming by the laser-based DED, where the nickel- and iron-based alloy powders and baseplates were used as the materials of concern. Different material combinations and parameter sets were set as controllable variables, with corresponding control groups created using the same material pairs. The macroscopic dynamic features of single-track forming under different material combinations, involving the melt pool's fluctuation, morphology, and dimension, were revealed using an *in situ* integrated high-speed camera. In addition, the multi-track and multilayer structures were fabricated by alternating the materials' deposition sequence, and microstructural characterization and microhardness measurements were used to quantitatively compare and analyze the differences in print quality of heterogeneous material combinations at the micro level. On this basis, combined with simulation, the printability differences induced by the dissimilarity in the material combination were better evaluated and elucidated. Finally, we also provide the limitations of the present investigation and possible directions for future work. The study aims to potentially guide more reliable DED forming of bimetallic parts based on the elaboration of the underlying printability differences in the deposition of different material combinations.

2. Experiments and methods

2.1. DED process and high-speed imaging

The deposition experiments were performed using a five-axis machine center (SVW80C-3D, Dalian Sunlight Technology Co., Ltd), which combines additive and subtractive hybrid manufacturing modules and consists of a fiber laser system (YLS-2000, 0–2 kW), a four-nozzle coaxial powder feeder (nitrogen as the protecting gas), a motion control and cooling system. The laser source with a beam waist diameter of 3 mm followed a Gaussian intensity distribution and scanned along the *x*-direction. During printing, a high-speed camera (5KF20, Fuhuang AgileDevice) was integrated into the DED system to *in situ* capture the track forming. The camera imaging with 5000 fps was placed in the *YZ* plane at an angle of approximately 60° to the *XY* plane (see figures 1 and S1). The camera was calibrated in advance and outputted images with pixels of 832 × 524, which were subsequently processed by in-house software.

2.2. Materials and parameters

Based on the study purpose (to investigate the deposition quality of different material combinations), nickel-based alloys, SS, and their combinations (pairs) were used as the representative experiment materials. As figure 1 shows, the roughly spherical IN718 powder (Nanjing Zhongke Yuchen Laser Technology Co., Ltd) with diameters between 20 and 180 μm was the raw material and was deposited onto three types of baseplates—IN718, IN625, SS316L—with 100 mm × 100 mm × 10 mm dimensions. Besides, control groups were set—using SS316L powder (Nanjing Zhongke Yuchen Laser Technology Co., Ltd) as the other raw material and printing it onto the three baseplates mentioned above. In addition, the bimetallic multi-track multilayer structures were fabricated using the combination of IN718 and SS316L, where each type of material was constructed with ten layers and eight tracks for each layer with an overlap rate of 50%. A round-trip scanning strategy was used for the inner layers (figure 1(a)). The powder's elemental composition is given in figure 1(d). The powder materials IN718 and SS316L are P1 and P2, and the baseplates IN718, IN625, and SS316L are B1, B2, and B3, respectively. For conciseness, the letter combinations are used in the following text to indicate the different material matching and their deposition relationships (e.g. P1B3 means the Powder—P1 (IN718) was deposited onto the Baseplate—B3 (SS316L)). The powder had been dried, and the surface of the baseplates had been cleaned prior to deposition.

To quantify the influences of the heterogeneity of material pair on the printing processibility and forming qualities, the same or different powder and baseplate matches were adopted to DED forming over a range of parameter sets. With the same energy density (*ED*), the powder feed rate (*F*) was set to five groups, i.e. 7.2 g·min^{-1}, 10.8 g·min^{-1}, 14.4 g·min^{-1}, 18 g·min^{-1}, and 21.6 g·min^{-1}. For a fixed powder feeding rate, different *ED*s were determined by varying the laser power and scanning speed (i.e. 23.8 J·mm^{-2}, 27.8 J·mm^{-2},

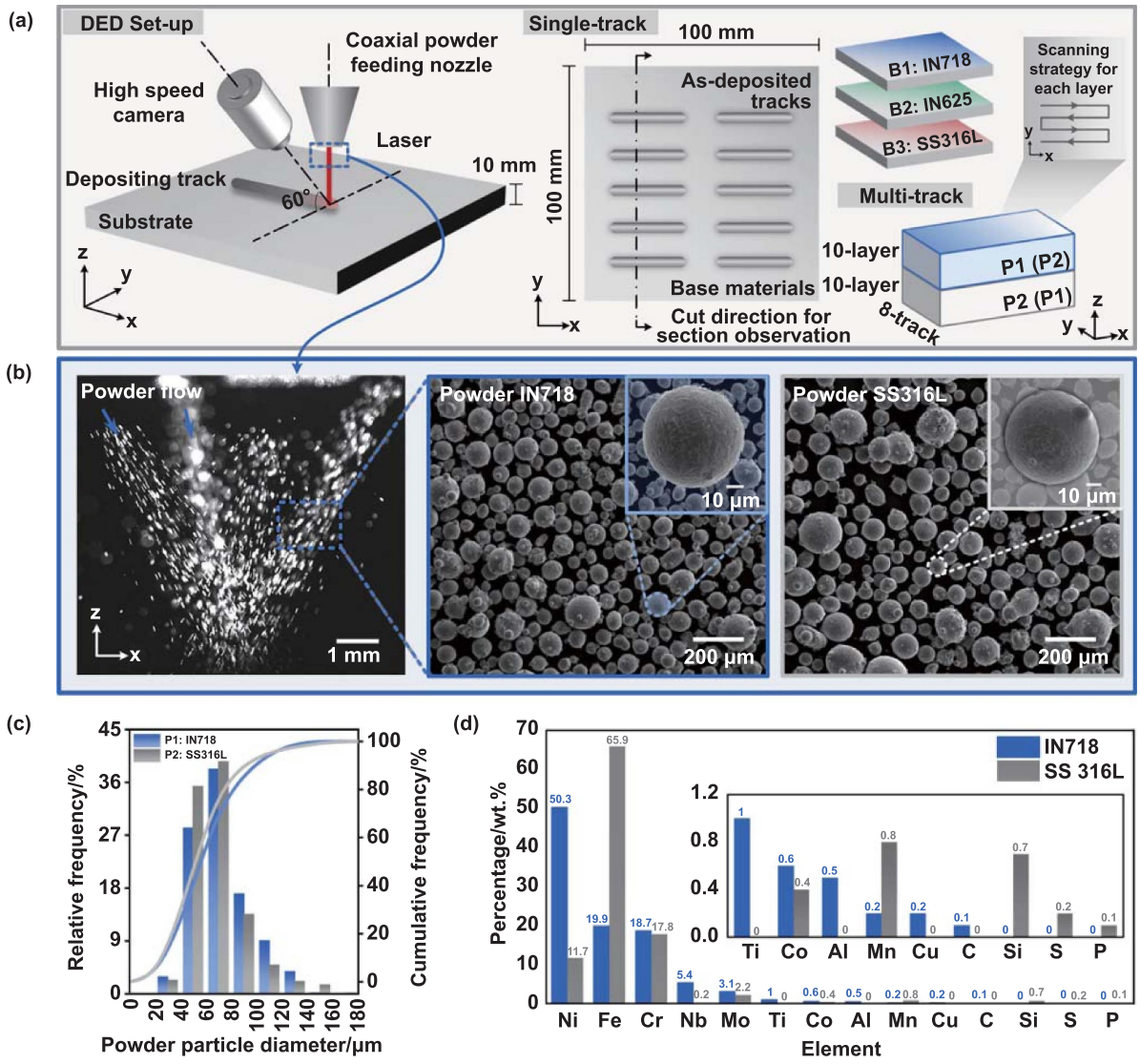

Figure 1. Experimental setup and materials. (a) Schematic of the DED process, where three types of base materials were adopted—B1 (IN718), B2 (IN625), and B3 (SS316L), and two types of powder materials were adopted—P1 (IN718) and P2 (SS316L). (b) *In situ* high-speed imaging of powder flow and the SEM images of IN718 and SS316L powder particle. (c) Powder size statistics, and (d) element composition of powder IN718 (P1) and SS316L (P2).

33.3 J·mm^{-2}, 40 J·mm^{-2}, and 46.7 J·mm^{-2}). In this study, the areal *ED* metric was used and evaluated as $P/(S \times d_0)$, where P is the laser power (W), S is the scanning speed (mm·min^{-1}), and d_0 is the diameter of the laser beam (3 mm). For the bimetallic structures, P-900 W, S-360 mm·min^{-1}, F-22 g·min^{-1} were used to build the IN718 layers, and P-800 W, S-300 mm·min^{-1}, F-22 g·min^{-1} were used for the SS316L layers. And the z-axis lift amount was uniformly selected as 0.4 mm.

2.3. Metallographic characterization and mechanical testing

The as-printed tracks were sectioned along the central section perpendicular to the scanning direction via the electrical discharge machining. All the samples were mounted first, ground with sandpapers (from #400 to #3000 sequentially), and polished with 1 μm diamond polishing compounds. The samples were then etched by a reagent (25 ml HCl + 25 ml C_2H_5OH + 2 g $CuCl_2$) to reveal the grain boundaries. A confocal laser scanning microscope was utilized to observe the track morphology. The metallographic characterization of the samples was performed using a SEM (Thermo Scientific), and the energy dispersive spectroscopy (EDS) spectra and maps were collected by an EDS detector (Ultim Max 40, Oxford Instrument) for the elemental analysis. Electron backscatter diffraction (EBSD) was performed on an SEM-focused ion beam setup (Symmetry S2, Oxford Instrument) with a 2.5 μm step size. An acceleration voltage of 15 kV was employed for EDS and EBSD. The Vickers hardness of the selected cross-sectional samples was measured using a digital hardness tester (HVS-1000 M) with a load of 200 g and a time of 10 s.

2.4. Modeling and simulation

In order to deeply understand and analyze the phenomenological results, a multi-physics CFD model was developed to simulate the deposition processes of single tracks with heterogeneous material pairs. The model was customized into the commercial software Flow-3D 2022R2 with a mesh size of 0.1 mm, and the mesh sensitivity was considered by conducting mesh convergence tests. The parameter sets used for the simulation were identical to the experimental conditions. The details regarding modeling methods and material properties are provided in the supplementary information.

3. Results and discussion

In this section, the experimental results are analyzed in detail from the perspectives of the printing process (i.e. the dynamic behavior of the melt pool during deposition) and the forming quality. Meanwhile, the multi-physics simulations are conducted to assist the theoretical interpretation of the experimental results to systematically know the differences in the printing performance of different material matches.

3.1. Melt pool behavior and track morphology

Operando imaging is a valuable real-time recording instrument in experimental investigation, particularly for AM involving multi-matter interactions in a short time [41, 42]. Here, the *in situ* high-speed imaging was implemented to visualize the transient complex physics during printing, including melt pool propagation and spatter features, which are closely related to the track solidification and formation.

The recorded images shown in figures 2(a)–(c) correspond to the situations that powder IN718 printed onto the baseplates IN718, IN625, and SS316L, respectively. Moreover, these exhibited frames with an interval of 0.5 ms and a duration of 1.5 ms are extracted from the stabilized deposition process. Some critical information (e.g. spatter trajectory, incident powder movement.) is marked. Combined with the video S1, it can be found that under the same parameter set, the melt pools of P1B1 and P1B2 fluctuate more dramatically than that of P1B3. At the same time, under the same *ED* and powder feeding rate, more spatters can be observed in the transient images of P1B1 and P1B2, and most of the spatters eject from the melt pool along the opposite direction of the laser scanning.

In P1B1, an incident powder particle p_1 with the gas flows from the nozzle outlet to the laser illumination range at a relatively high speed and contacts with the melt pool at the $(t_0 + 1)$ ms, afterward causing a large 'ripple' on the melt pool surface due to the rapid melting and strong impact (the last frame in figure 2(a), and video S2). From the images of P1B2, the unevenness on the melt pool's upper surface looks like the boiling water's surface, caused by the impinging from the incident powder and the recoils of the metallic vapor inside the melt pool due to the localized intense energy. Ignoring the mass difference among individual powder particles, we assume that the powders were to the deposition area with the same incident velocity under a specific feeding rate and their gravity. When the incident powders land on and hit the surface of the melt pool at a certain initial velocity, they impact the surface tension of the melt pool. Simultaneously, some molten droplets are ejected from the molten pool in the form of jet spatters due to localized boiling [43]. From figures 2(a) and (b), intense flow and a higher occurrence of splattering are notably evident in the homogeneous material combinations P1B1 and P1B2. By comparison, the melt pool of P1B3 behaves relatively smoothly and peacefully and is accompanied by sparse spatters (figure 2(c)). By comparison, the melt pool of P1B3 behaves relatively smoothly and peacefully and is accompanied by sparse spatters (figure 2(c)). According to the simulation results, P1B1 and P1B2 have more $+z$-directed streamlines at the front of the melt pool, while on the contrary, the P1B3 behaves differently, with more streamlines driven by the Marangoni effect moving from the laser center to the back of the melt pool on both sides. These results are consistent with and confirm the findings from the imaging observations, indicating that, compared to the heterogeneous material combination P1B3, the homogeneous material combinations (P1B1 and P1B2) exhibit stronger convection within the melt pool and more pronounced surface fluctuations with significant boiling effect. The viscosity of the liquid materials plays an essential role in the resulting melt flow stability. A highly viscous material may bring about a reduction in fluid velocities and further impede the convection in the melt pool, while a lower viscosity can promote the flowability [44]. Considering that the SS316L has a higher viscosity than IN718 and IN625, its combination shows a more stable flow motion and looks 'calmer' than the other two groups.

Furthermore, intense melt flow corresponds to a larger melt pool size. By extracting the edge features of the melt pool (figure 2(d)), it is easy to observe that the melt pool profiles are relatively large when depositing IN718 powder onto similar base materials (the blue and green irregular curved circles, P1B1 and P1B2), while the melt pool trailing along the x-direction is longer and relatively narrow for the case that used baseplate of SS316L (the red irregular curved circle, P1B3). Correspondingly, the postmortem inspection shown in figure 2(f) indicates that IN718 deposited on the baseplates of IN718 and IN625 presents a larger track cross-section than that deposited on SS316L. In addition, the surface morphology of deposited tracks printed with different material pairs exhibits variety. The track surfaces of IN718 deposited on disparate baseplates were covered with non-uniform severity of powder adhesion. On the track surfaces of P1B1 and P1B2 (the first two sub-figures in figure 2(e)), massive agglomerations of partially melted powders remain, which may result from the relatively severe spatter ejection and their oxidation and resolidification falling on the solidified tracks during the deposition [45, 46]. By contrast, the surface of P1B3 also stocks visible unmelted particles; however, they are adhering more individually and loosely.

The above images recorded at a specific parameter condition suggest the morphology differences of the melt pool for different material matches. The melt pool size and shape result

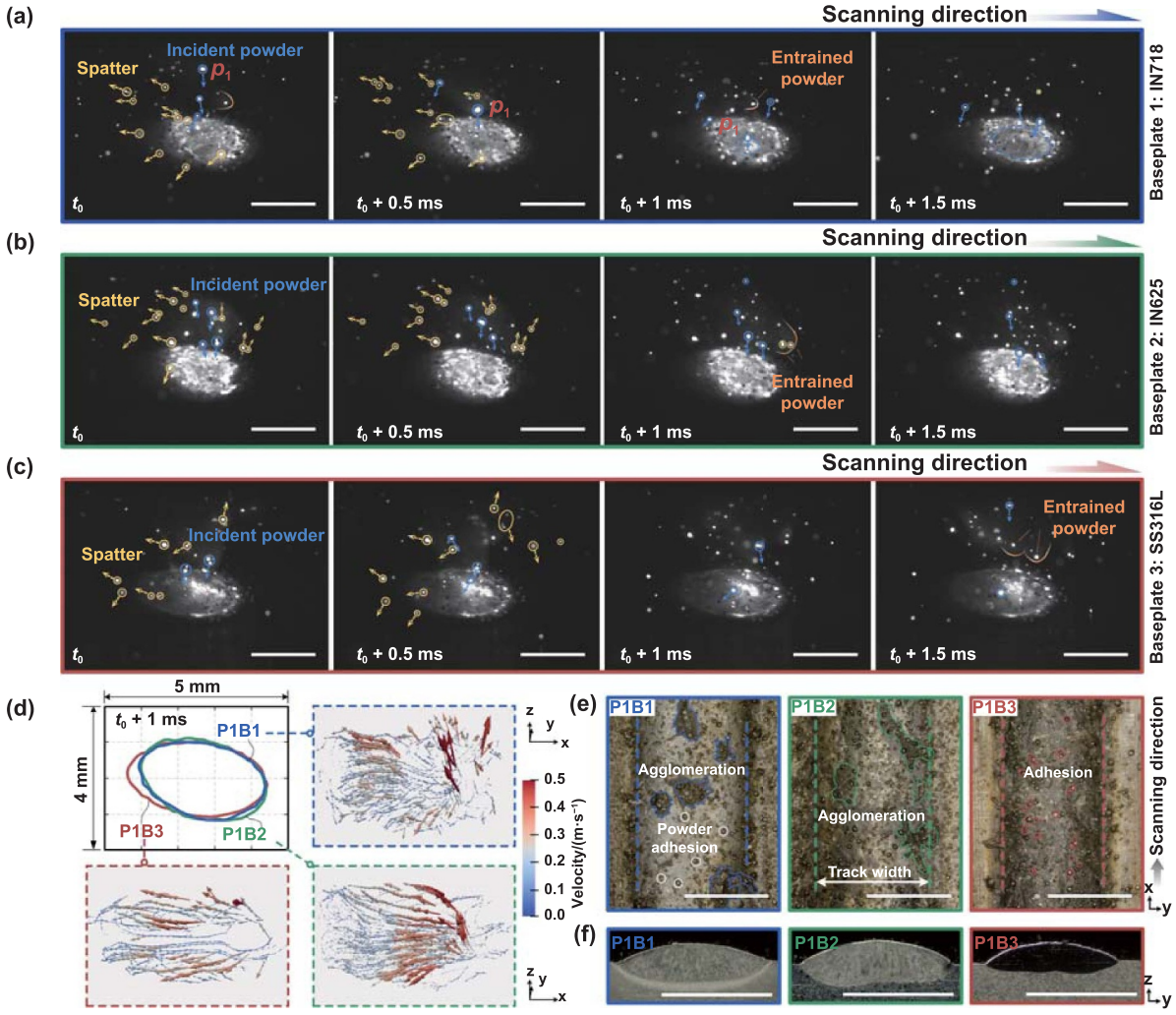

Figure 2. Deposition process and the track morphology. (a)–(c) Display the *in situ* captured tableaux of melt propagation and some physical features during depositing for P1B1, P1B2, and P1B3, respectively. (d) The profiles of the melt pool at a frame of $(t_0 + 1)$ ms, and the flow streamlines in the molten pool of each case. (e) The outer surface of the formed tracks, in which the colored arrows mark the scanning direction. (f) Cross-section of the tracks. The parameter set used for *in situ* imaging was P-1000 W, S-600 mm·min^{-1}, F-18 g·min^{-1}. All the scale bars are 2 mm.

from the process parameters [39, 47, 48]. We further investigated the melt pool's dimension of each material pair with different parameter sets. Figures 3(a) and (b) shows the effect of altering the powder feed rate and *ED* on the aspect ratio of the melt pool (d w^{-1}), where the *ED* refers to the areal energy density, as detailed in section 2.2. When the *ED* is controlled as 33.3 J·mm^{-2}, d w^{-1} shows a decreasing trend for all material combinations as the powder feed rate increases. P1B1 pair has the smallest reduction of d w^{-1} value, suggesting that the dimension of the melt pool generated by this material match is relatively stable with the powder feeding variation. Interestingly, the melt pool aspect ratio of P1B3 pair is generally smaller than that of the other two pairs with similar material matches (P1B1 and P1B2). The fluctuations of the melt pool dimension for P1B3 at the powder feeding rate of 18 g·min^{-1} are more sensitive to the given *ED* variation, while for the first two pairs, the dimension changes of their melt pools are relatively slight, reflected by a stable value of d w^{-1} nearly ∼0.14 (figure 3(b)).

Within the given parameter window, the small d w^{-1} values imply that the melting process followed a conduction mode for all material combinations [41, 49], ensuring that the tracks were generated in a relatively stable regime. Further quantitative analysis indicates that the melt pool width or depth alone is affected by material match heterogeneity. The increasing powder feeding rate (F) leads to a reduction of the melt pool width for P1B1 and P1B2, while it brings an inconspicuous effect on the width of the melt pool of pair P1B3 (i.e. the width change in figure 3(c)); a larger powder feeding means that more particles entering the laser irradiation area, which increases the refractive degree and the energy attenuation due to the shielding effect [50, 51], thus weakening the penetration ability of the incident laser, further leading to the reduction of the melt pool depth (i.e. the depth change in figure 3(f)). In addition, the results in figures 3(d) and (e) show that increasing the laser power (P) alone induces wider printed tracks with deeper melt pool depths while improving the scanning speed causes a reduction in the width and depth of the melt

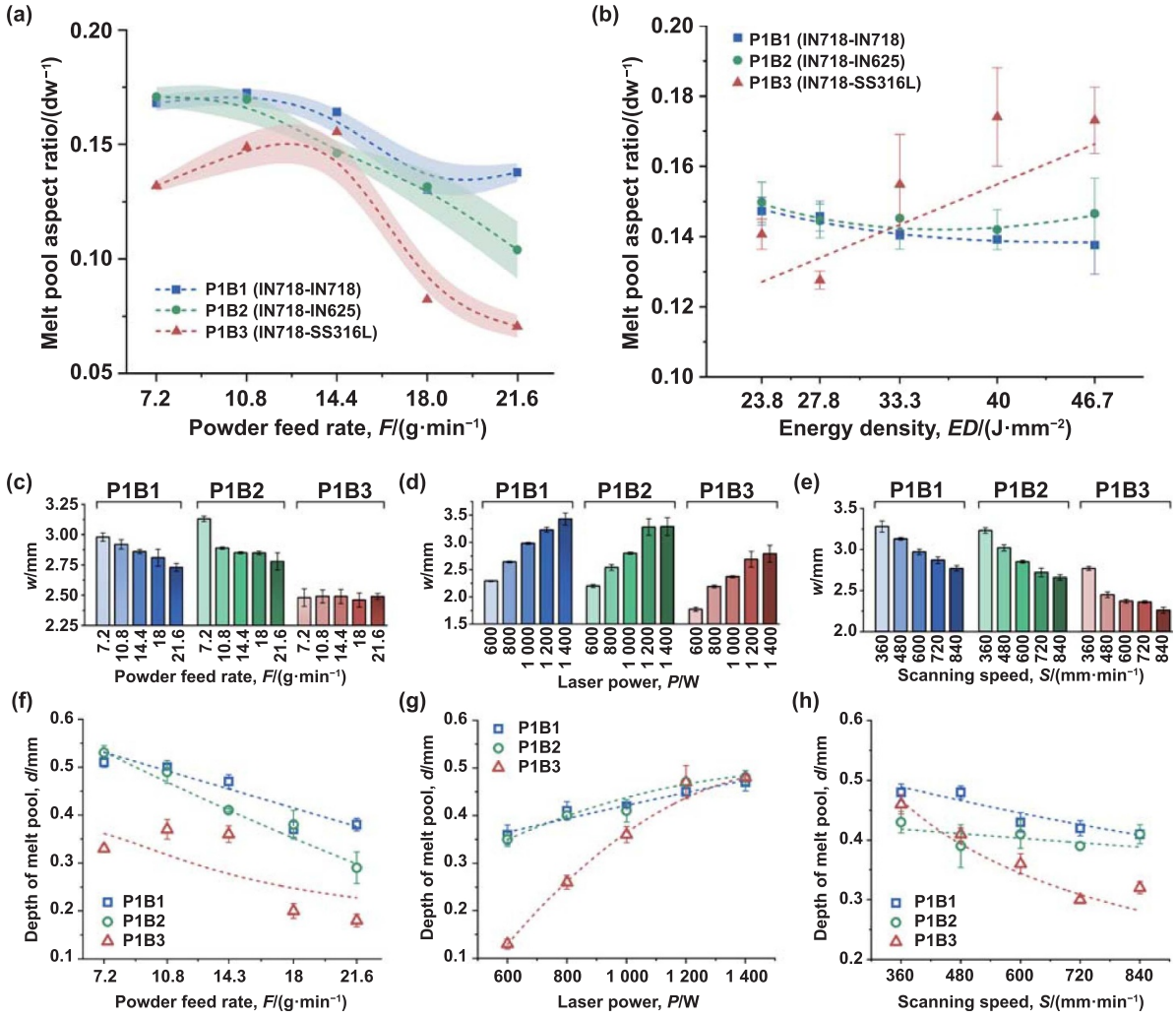

Figure 3. Melt pool dimensions. Figures (a) and (b) show the changing melt pool aspect ratio (d w^{-1}) trend with the increase of *F* and *ED*, respectively. (c)–(e) Illustrate the variations of melt pool width (w) with the change of *F, P*, and *S*, respectively. (f)–(h) Illustrate the variations of the melt pool depth (d) with the change of *F, P*, and *S*, respectively.

pool. Laser power and scanning speed are the dominant factors for modifying *ED*; thus, the variations of both are based on the change of *ED* to affect the melt pool size—*ED* is positively correlated with the altering in power, while reversely, with scanning speed changing, and the effect of laser power is more significant. It is worth noting that the melt pool width and depth of IN718 powder deposited on a dissimilar base material are more sensitive to changes in the above parameters. For instance, the melt pool depth of P1B3 increases notably when turning the power from 600 to 1400 W (figure 3(g)). Still, the melt pool size of P1B3 is generally smaller than that of P1B1 and P1B2. The Marangoni convection, as the dominant driving force for melt pool propagation, will affect the clad geometry, where the convection intensity can be quantified by tracing the speed and directions of the melt flow [52]. As aforementioned, the streamlines of homogeneous material combinations (P1B1 and P1B2) are thicker than that of the heterogeneous material combination (P1B3), suggesting a stronger melt flow for the formers, which corresponds to the results that a relatively large melt pool size is generated for the homogeneous material combination. In addition, the distinctions in melt pool size are also related to the thermal physical parameters of the base materials [53]. The melting point and specific heat of B3 (SS316L) are higher than that of B1 and B2 (IN718 and IN625). With the same parameters, the heat supplied by the laser beam (excepting the energy dissipation by powder shielding) may be insufficient to melt B3 while enough for B1 and B2, leading to a relatively weak penetration capability. SS316L has a higher thermal conductivity below the solidus temperature compared to IN718 and IN625. Thereby, at the same ambient temperature, when the heat is delivered to the three baseplates of the same physical dimension, relatively fast heat diffusion would happen on B3, which causes more wasted energy that would otherwise be used for forming the melt pool, resulting in a narrower and shallower melt pool for P1B3. This confirms the relatively small cross-section of the track of the P1B3 combination shown in figure 2(f).

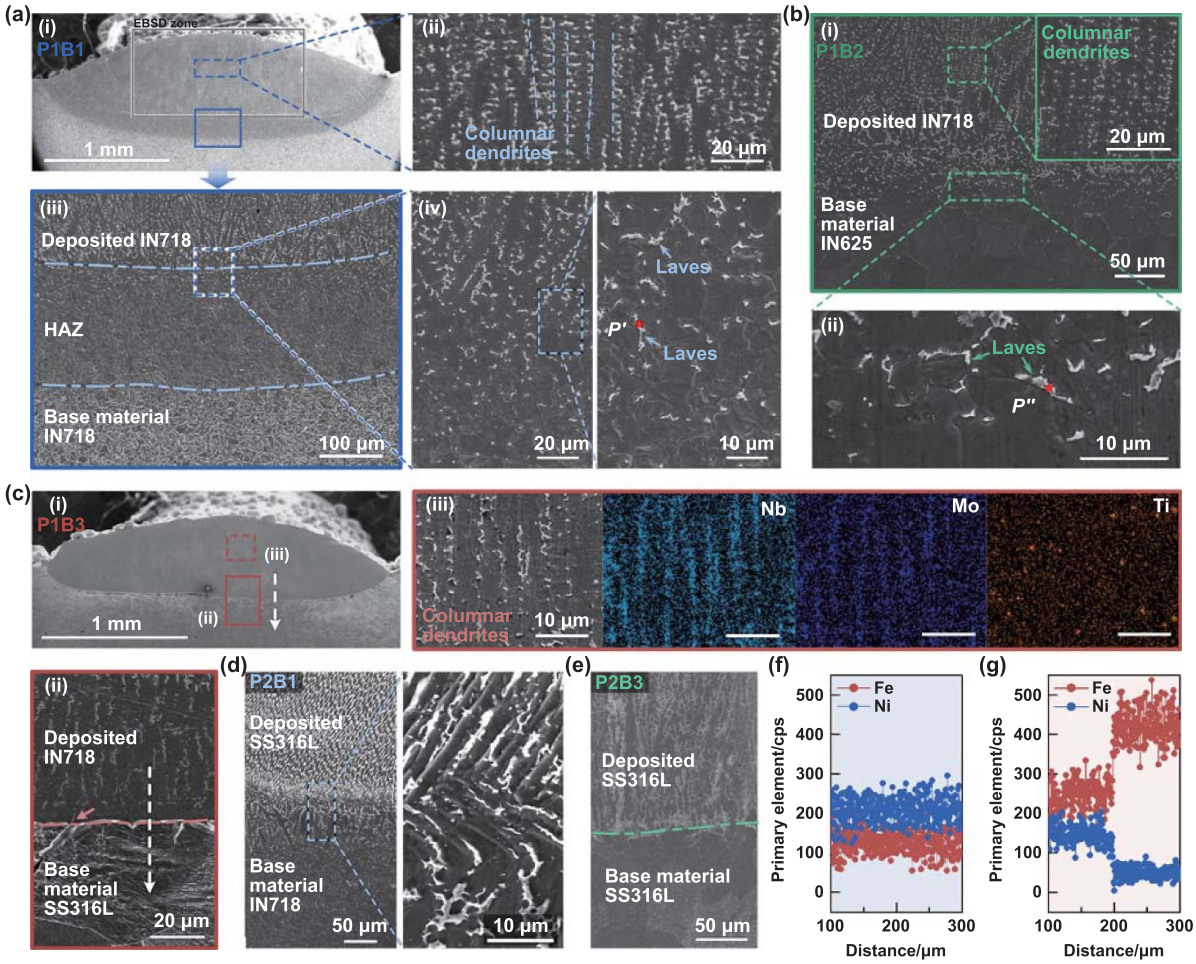

Figure 4. Microstructural morphology of different material combinations. Figure (a) is for the P1B1, where (i) is the global SEM image, (ii) is the zone of the deposited layer, (iii) is the magnified interfacial zone marked with the solid blue rectangle in (i), and (iv) the localized magnification of the interface. Figure (b) is for P1B2, where (i) is the interfacial microstructure and (ii) is the corresponding localized magnification. Figure (c) is for P1B3, where (i) is the global SEM image, (ii) is the magnification of the interface, and (iii) is a localized magnification of the deposited layer and the corresponding EDS mapping of Nb, Mo, and Ti. Figure (d) is the interface morphology of P2B1. Figure (e) is the interface morphology of P2B3. Figure (f) is the primary element (Fe and Ni) variations with the distance, where the sampling direction is shown as the white dashed arrow in (a-iii). Figure (g) is the primary element (Fe and Ni) variations with the distance, where the sampling direction is shown as the white dashed arrow in (c-ii). The parameters used for these groups were P-1000 W, S-600 mm·min^{-1}, F-18 g·min^{-1}.

3.2. Microstructure morphology and features

3.2.1. Interface and microstructure morphologies. From the perspectives of internal and microscopic levels, the microstructure of the samples printed with different material matches shows diversity. On the one hand, it embodies the microstructural morphology, and the difference in morphology at the interface between the deposited layer and the base material.

A HAZ between the deposited layer and the substrate can be observed when IN718 powder was deposited on the nickel-based alloy baseplates (figures 4(a)–(i)), whereas it is a sharp transition for the combination of P1B3 (figure 4(c)). Generally, the HAZ arises from the deposition's thermal cycling and heat accumulation, and its range is strongly influenced by the material characteristics [54]. With the same heat input, when SS316L was used as the base material, relatively more heat would dissipate due to its relatively large specific heat capacity and thermal diffusion capability (compared to IN718 and IN625), and the accumulated heat in the substrate may not be sufficient to affect the generation of an apparent HAZ. Meanwhile, from the view of materials' properties, the solidification temperature ranges of IN718 and SS316L are different. The former's (1336 ˚C–1260 ˚C) is lower than the latter's (1460 ˚C–1420 ˚C) [55]. During cooling, the SS316L as the base material would solidify prior to the melts of IN718 despite the occurrence of the composition mixture in the melt pool evolution, so a direct transition for the material combination of P1B3 was yielded. In addition, the solidification interval (SI) is related to the generation of solidification cracks and a positive correlation between them [56]. The melts of IN718 alloy own a relatively wide SI compared to the base material SS316L, so the risk of cracking at their interface is higher. This can explain the appearance of the microcrack at the boundary between

the deposited layer and the baseplate (figure 4(c-ii)). Even for the material pairs using SS316L powder, the difference in the properties of the base materials can rationalize the sectional morphology of P2B1 and P2B3 pairs, where the former appears as a 'filamentary' transition layer near the interfacial zone (figure 4(d)), while the latter has a sharp interface between the deposited layer and the baseplate (figure 4(e)). The interfacial morphology is also consistent with the changes in composition near the melt pool interface. The content of principal elements (Fe and Ni) near the interface of the homogeneous material combination P1B1 did not show significant changes (figure 4(f)); in combination P1B3, where no significant HAZ was observed, there was an apparent increase trend of element Fe from the melt pool to the substrate, while the content of the element Ni, on the contrary, decreased significantly (figure 4(g)). In the case of the material pair where SS316L was the powder material, the clear interface also corresponded to the variation of the primary elements (figure S3).

Furthermore, the interfacial morphology of the multi-track bimetallic structures also varies with the deposition sequences of the different material combinations. In the cross-sectional direction perpendicular to the scanning direction, namely the *y*–*z* plane, a distinct interface is obtained when the IN718 was deposited first followed by SS316L (i.e. P2/P1, figure 5(b)); in contrast, the interface of the material combination in which SS316L was deposited first followed by IN718 was an irregular transition, and the distribution of the primary element Fe was inhomogeneous (i.e. P1/P2, figure 5(c)). The reason for this difference is that the P1 material (IN718) has a higher viscosity and density compared to P2 (SS316L). When it is used as a base material (referring to the P2/P1 combination), it is not conducive to the composition mixing within the melts.

In terms of the microstructures near the interfaces, the granular precipitates are discretely distributed near the HAZ or the transition zone between the deposited layer and the base material in samples P1B1 and P1B2 (figures 4(a-iv) and (b-ii)). Combined with the EDS analysis (figure S4), they are inferred to be the Nb- and Mo-rich Laves phases. However, for P1B3 (figure 4(c-ii)), the direct interface is surrounded by only a small amount of discrete and particle-like precipitates, and their distribution is influenced by the incomplete mixing of IN718 powder material with the SS316L base material. The microstructures within the deposited layers show a similar morphology along the deposition height direction (i.e. the *z*-direction) for the clad layers of P1 (IN718) powder printed on three baseplates. From figures 4(a-ii), (b-i) and (c-iii), it can be observed that the middle areas of the deposited layers of P1B1, P1B2, and P1B3 uniformly consist of columnar dendrites, whose growth directions are all vertically upward following the direction of the temperature gradient and are dominated with austenitic matrix and strip- or chain-like structure spliced by continuous Laves phases.

3.2.2. Grain and crystallographic features. The crystallographic features of the deposited layers are dissimilar, which is the other reflection of the microstructural diversity for different material combinations. EBSD analysis was conducted on the samples printed using different material pairs, where the texture evolutions concerning the deposited layer were examined on the *YZ* plane to further assess the potential differentiation. Figures 6(a) and (b) exhibit the IPFs in the laser scanning direction for the combination P1B1 and P1B3, where the specific location of each group displayed corresponds to the boxed area shown in figures 4(a)–(i).

For the deposited layers of the single tracks, the columnar grains are the main structures for P1B1 and P1B3. The shape in P1B1 is of uniformity relatively, while in contrast, the coarse columnar grains with a larger aspect ratio predominate in P1B3, especially in the middle zone; a proportion of equiaxed grains are densely distributed at the top of the cladding layer. Also, the grains in P1B3 have a preferential growth direction of <001>. According to figures 6(e) and S5, it is revealed that the grains in the deposited layer of P1B1 and P1B2 do not exhibit a preferred orientation, whereas a slight fiber texture in [100] with the maximum MUD of 4.72 shows in the P1B3. This preferred growth orientation is common in IN718 materials solidified in FCC structures, and similar results have been reported in related studies [57, 58]. For the combinations of P2, the coarse columnar grains predominate in the P2B1 deposition layer, and a very small fraction of equiaxed grains are confined to specific regions at the top of the layer (figure 6(c)), whereas P2B3 consists of irregular columnar grains extending throughout the clad layer (figure 6(d)). And the grains in the combinations of P2B*X* appear as random crystallographic textures (figures 6(f) and S5).

It is noteworthy that the grains within the clad layer show a tendency to transition from columnar dendrites in the middle zone to equiaxed dendrites in the top zone, which is relatively more pronounced in the heterogeneous material combinations (P1B3 and P2B1). Taking the case of P1B3 as an example, as mentioned earlier, less spatter was generated during the melt pool propagation. Relatively more powder entered the melts and contacted the melt pool, resulting in a relatively high deposition height (figure 2(f)); the unmelted powders contacting the top of the melt pool increase the possibility of heterogeneous nucleation. Meanwhile, the equiaxed grains on the top of the clad layer might be the microstructure of the raw powder itself trapped by solidification at the top of the melt pool [43, 59]. Moreover, referring to the degree of alloying (DoA) [60] to quantify the content of specific elements is helpful to realize the interdiffusion extent between the powder and the base materials and to further evaluate the microstructure within the heterogeneous combinations. Referring to the DoA scheme (table S3 and Supplementary text B), the DoA value of the examined melt pool's cross-section shows a majority level, indicating that the temperature gradient and the composition dominate the grain growth. On the one hand, the grain growth along the gradient direction tends to form elongated columnar grains in the middle zone; on the other hand, the large interdiffusion of Fe causes an uneven solute distribution, further leading to a certain extent of constitutional supercooling [61], which is conducive to promoting the transition from columnar to equiaxed grains, as shown in the upper zone of the clad layer.

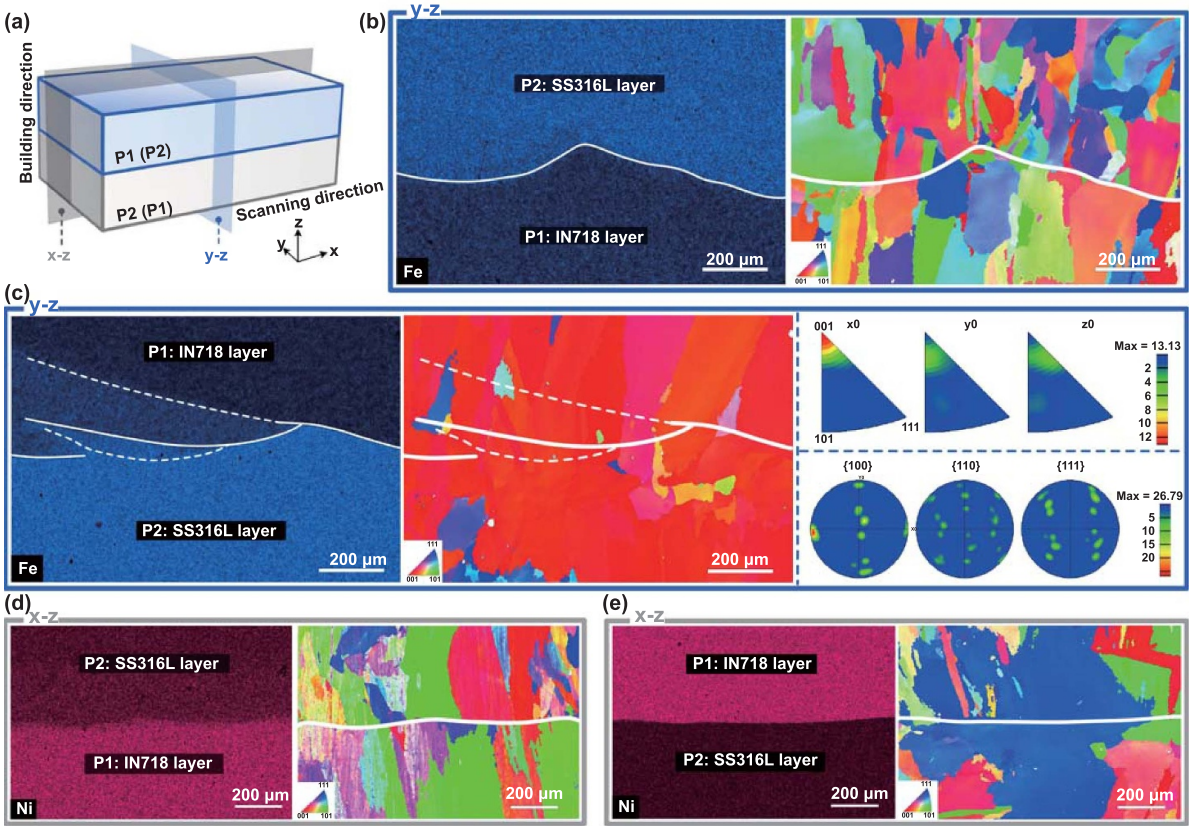

Figure 5. Interfacial differences between the multi-track structures fabricated with different material combinations. (a) Illustration of the bimetallic structures, where P1/P2 means the upper part as P1 and the lower part as P2, and P2/P1 means the upper part as P2 and the lower part as P1. (b) Interface features of the P2/P1 material combination in the *y*–*z* plane. (c) Interface features of the P1/P2 material combination in the *y*–*z* plane. Figures (d) and (e) are the interfacial features exhibited in the *x*–*z* plane for P2/P1 and P1/P2, respectively.

Grain size statistics for clad layers of single tracks can illustrate differences in microstructural features. Based on the quantitative analysis (figure 6(g)), the grains in P1B1 and P1B2 have the highest relative frequency in the 10–20 μm interval, while the grains in P1B3 are concentrated in the 20–30 μm range within a limited count of statistics and P1B3 contains more grains with the relatively large size (70–160 μm). Correspondingly, the mean grain value for P1B3 (34.2 μm) is larger than that of the other two groups (23.5 μm for P1B1 and 30.3 μm for P1B2, figure 6(h)). For the combinations with SS316L (P2), the statistical result in figure 6(i) shows the total grain size range, and the mean grain size of P2B1 (57.5 μm) is larger than that of P2B3 (37.3 μm). Although the grain size distribution range of the combination P2B2 is similar to P2B3's, its corresponding mean value is relatively large.

For the multi-track bimetallic structures formed by P1 and P2, grain growth exhibits differences in the region of interfaces induced by heterogeneous materials. For the P2/P1 combination, the direct interface limits epitaxial grain growth, and the grains near the interface are irregular in shape and do not exhibit a clear preferred growth direction (figures 5(b) and (d)). For P1/P2, the upper IN718 grains show epitaxial growth based on the lower 316 l grains and exhibit a distinct <001> growth orientation along the deposition height direction, leading to the formation of thicker columnar grains; the grains are still epitaxially grown despite the elemental variation in the *XZ* plane (figure 5). Essentially, differences regarding the grain growth features at the interface of the bimetallic structure are related to the interface formation mechanism of the alternate deposition of the Ni- and Fe-based materials. As mentioned before, a gradual transition interface was generated for the P1/P2 combination. When depositing IN718 on the SS316L layer, the solidification started from the previously solidified SS316L and the newly formed liquid solute, and due to the change in solute composition generated when the dissimilar materials are combined, constitutional undercooling occurred at the solid/liquid front [62], thus promoting dendrite growth, which further evolved into columnar grains formed in an epitaxial growth pattern across the interface and in the newly deposited IN718 layer.

As for the P2/P1 combination, a significant compositional mutation was observed at the interface. The grains of the previously deposited IN718 layer would grow in an epitaxial trend within the layer. Subsequently, depositing SS316L on it, the initial solidification of the new solute happened in the composition change zone, and an unconventional melt pool flow would occur, which was validated by Xiao *et al* [63]. With a large undercooling, the special flow promoted a large number of nuclei, resulting in the mixed grain structures without epitaxial growth. Accordingly, the grain features near the P2/P1 combination interface differ from those of the other combination.

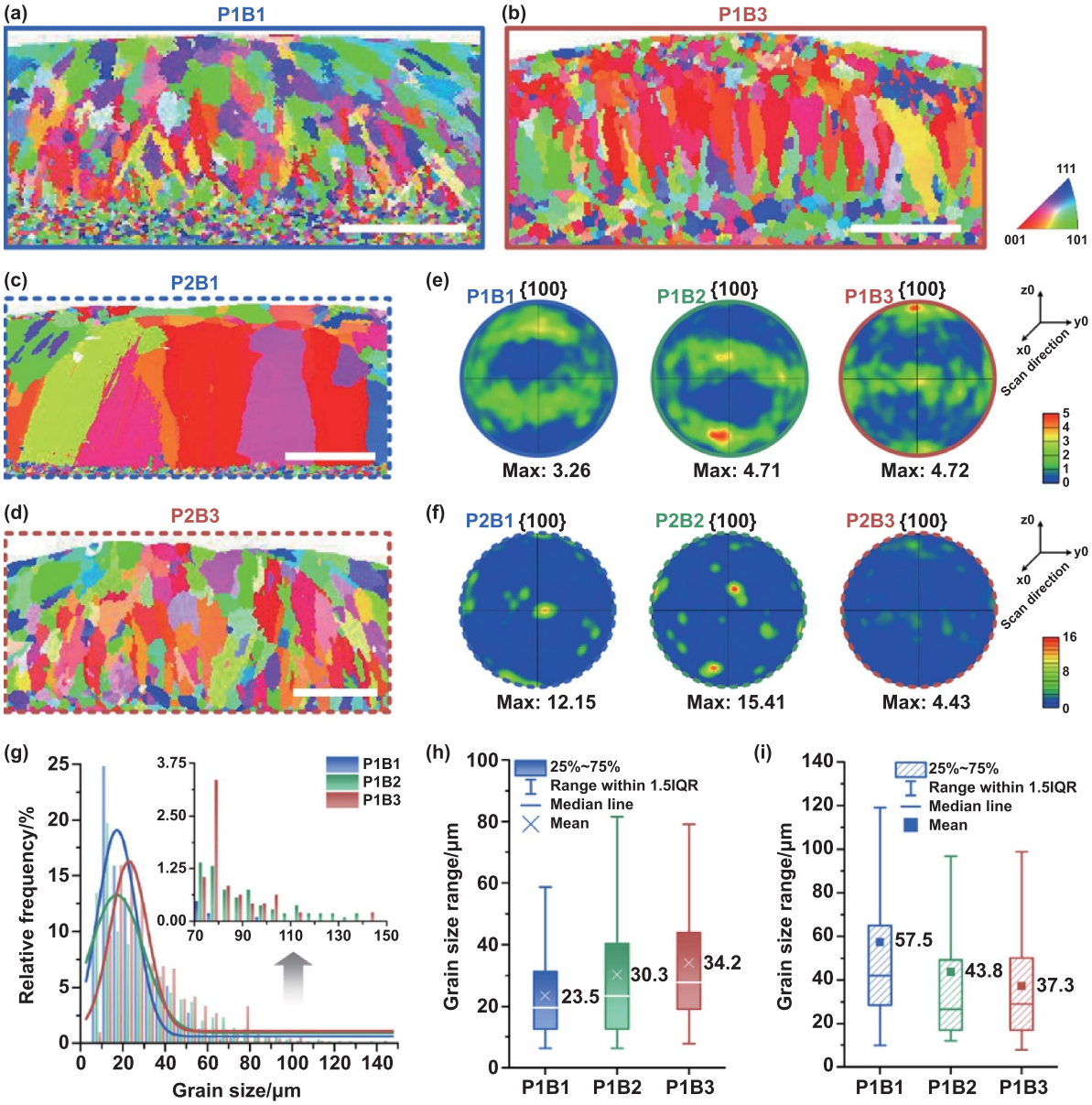

Figure 6. Crystallographic information of the single tracks printed with different material combinations. Figures (a) and (b) are the locally inverse pole figures (captured along the section plane, i.e. *YZ* plane) of P1B1 and P1B3, respectively. Figures (c) and (d) are the local IPFs of P2B1 and P2B3, respectively. Figure (e) is the {100} contoured pole figures of P1B*X*, and (f) corresponds that of P2B*X* ($X = 1, 2, 3$). Figure (g) is the grain size distribution of sample P1B*X*. Figure (h) is the grain size statistics of samples of P1BX (P1B1: $n = 689$; P1B2: $n = 714$; P1B3: $n = 477$), and (i) is that for P2BX (P2B1: $n = 168$; P2B2: $n = 225$; P2B3: $n = 464$). The parameters used for these groups were: P-1000 W, S-600 mm·min^{-1}, F-18 g·min^{-1}. All the scale bars stand for 250 μm.

3.3. Microhardness comparison and analysis

Microhardness is a vital index of mechanical property that can synthetically display materials' elasticity, plasticity, and strength [64]. In order to uncover the difference in the microhardness, partition tests were performed on the samples printed with different material combinations. The cross-section of the printed track could be roughly divided into three zones of interest (ZOIs) through the D-S boundary and the M-S junction, namely the EZ, PZ, and BZ (figure 7(a)). Ten points were selected evenly in each ZOI to obtain the hardness values.

Concerning the tracks printed with different material matches (same powder, different baseplates), the hardness values within the same area of concern are unlike, as shown by the fact that the powder P1 and P2 deposited onto the same two nickel-based alloy baseplates have similar hardness values, yet are significantly higher than those deposited onto SS baseplate. Based on the microhardness statistics in figure 7(b), the average microhardness (Ave. $HV_{0.2}$) of each ZOI for P1B1 and P1B2 are >10% larger than those of the corresponding zones for P1B3; comparably, for the former two pairs (P1B1 and P1B2), the Ave. $HV_{0.2}$ of each zone is close,

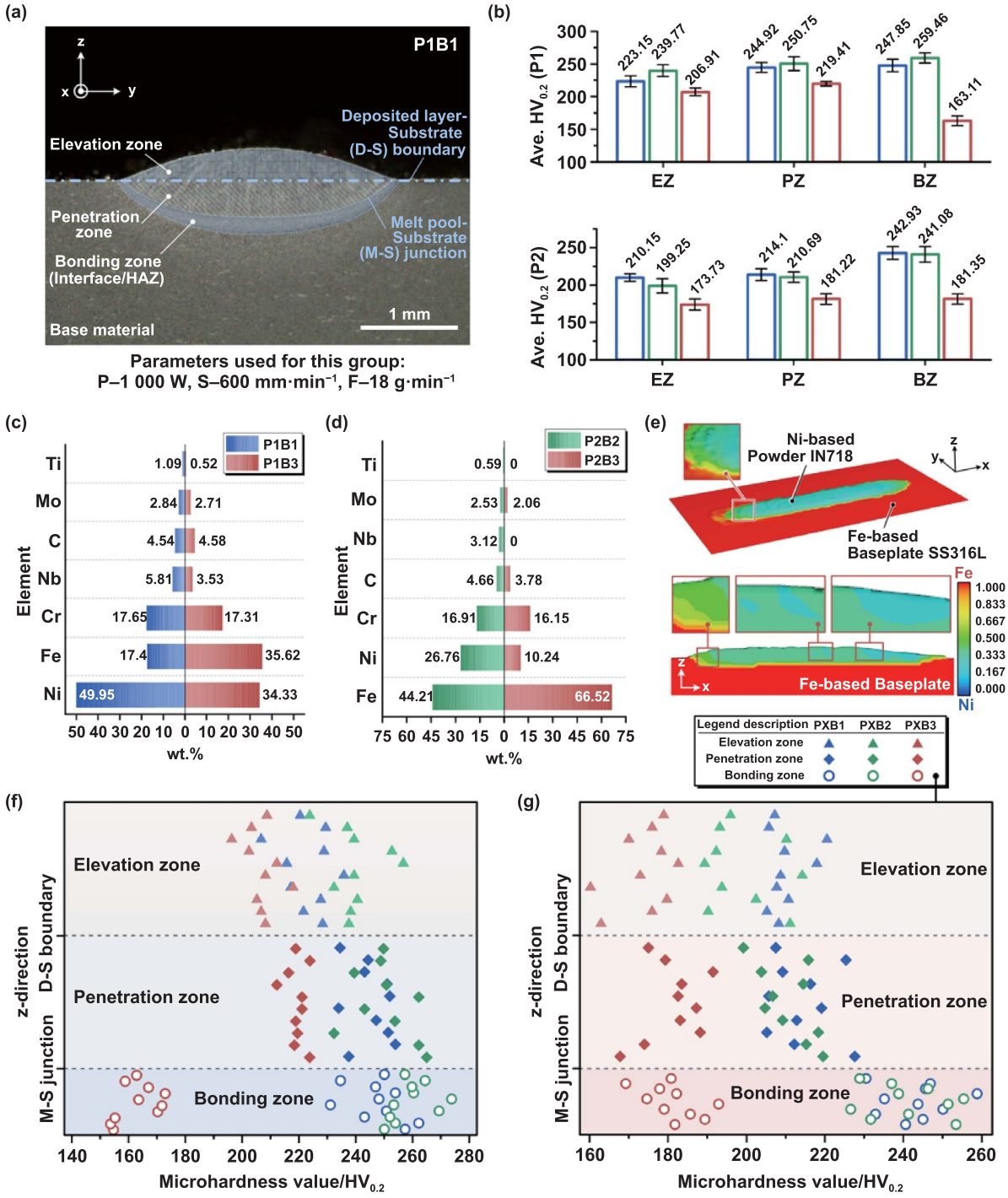

Figure 7. The microhardness comparison for different material combinations. (a) Illustration of region division in the sample; (b) the average regional microhardness values vary with the material combination; (c) the contents of main elements in the deposited layers of pairs P1B1 and P1B3; (d) the contents of main elements in the deposited layers of pairs P2B2 and P2B3; (e) the simulated results of the principal element distribution for combination P1B3 that matched Ni-based powder (IN718) and Fe-based base material (SS316L); (f) scatters of microhardness value in different ZOIs for combinations of the IN718 powder with different base materials; (g) scatters of microhardness value in different ZOIs for combinations of the SS316L powder with different base materials (p.s. blue-colored symbols are for the P*X*B1, green for P*X*B2, and red for P*X*B3. ($X = 1, 2, 3$)).

approximating the previously reported value of as-deposited IN718 (∼255 HV) [65]. A similar trend also shows in the P2BX combinations, where a negligible difference between the average microhardness values in each ZOI of P2B1 and P2B2 appears (∼210 $HV_{0.2}$ for EZ and PZ, ∼240 $HV_{0.2}$ for the BZ), and their hardness values exceed >15% than the values

in the same zones of the combination P2B3, and the latter nearly agree with the value of deposited SS316L reported by the earlier study (∼182 HV) [66].

Grain size refining has a specific impact on the hardness, quantified by the Hall–Petch relationship [66], namely a smaller grain size corresponding to higher yield strength and hardness. As discussed earlier (figure 6(h)), the grain of the P1B1 is finer than that of P1B3 on average, which can be aided in understanding the result of its higher hardness. Meanwhile, the elemental composition also influences the hardness, and its influence can be dominant and even greater than the grain size or the dendritic arm spacing, verified by the study of Wolff *et al* [67].

Disparities in the distribution of elemental composition in the different printed layers can rationalize the differences in hardness among the different material matches. For the tracks printed with nickel-based powder (P1), the equivalent Ni element (Ni_{eq}) can correlate with the changing trend of microhardness values; it has been investigated that there is a quantitative linear relationship between them [68]. Focusing on pairs P1B1 and P1B3, and referring to the EDS analysis in figure 7(c), it can be calculated by equation (1) that the Ni_{eq}—135.7 for P1B1 with Ni-based alloy as the base material is greater than the Ni_{eq}—122.5 for P1B3, which is the combination with an iron-based material as the base material (figure S7). A greater equivalent Ni element fits with a better hardness property. Accordingly, it ties nicely with the results that pair P1B1 exhibits a superior hardness compared to pair P1B3,

$$\begin{aligned} \mathrm{Ni_{eq}} = {} & \mathrm{Ni} + 0.65\mathrm{Cr} + 0.98\mathrm{Mo} + 1.05\mathrm{Mn} + 0.35\mathrm{Si} + 12.6\mathrm{C} \\ & - 6.36\mathrm{Al} + 3.80\mathrm{B} + 0.01\mathrm{Co} + 0.26\mathrm{Fe} + 7.06\mathrm{Hf} \\ & + 1.20\mathrm{Nb} + 4.95\mathrm{Ta} + 5.78\mathrm{Ti} + 2.88\mathrm{W}. \end{aligned} \tag{1}$$

Likewise, regarding the matches of SS316L powder (P2), the difference in hardness can be examined by the elemental composition. Previous studies have demonstrated that an approximation of steel's hardness can be estimated by the chemical composition, where the critical weldability (P_{cm}, equation (2) was referred, and its value for iron-based alloys has a linear relationship with the hardness value of the corresponding material—larger P_{cm} corresponds to greater hardness [69]. Given that, taking pairs P2B2 and P2B3 as examples and combining the element analysis of printed layers (figure 7(d)), the P_{cm} for P2B2 can be calculated as 6.16, which is greater than the corresponding value of 4.95 for P2B3 (figure S7). The magnitude relationship between P_{cm} values of the two pairs quantitatively supports the outcome that the hardness of the stainless-steel powder deposited onto the nickel baseplate is superior to that onto the stainless-steel baseplate,

$$P_{cm} = \mathrm{C} + \frac{\mathrm{Si}}{30} + \frac{\mathrm{Mn} + \mathrm{Cu} + \mathrm{Cr}}{20} + \frac{\mathrm{Ni}}{60} + \frac{\mathrm{Mo}}{15} + \frac{\mathrm{V}}{10} + 5\mathrm{B}. \tag{2}$$

It is noted that the differentiation of hardness values herein is not simply epitomized as whether a match with the same materials outperforms a different material match. For the tracks printed with a specific parameter set, the dissimilarity in the composition of the powders and baseplates can directly influence the difference in hardness performance. More specifically, the dominant roles were the mass transformation and elemental intermixing between heterogeneous materials (powder and baseplate) accompanied by the dynamic behaviors of the melt pool (fluctuation, propagation, and solidification) during deposition. When using nickel-based powder, a portion of Fe from the iron-based baseplate would be certainly blended into the deposited layer following the melt flow mainly governed by Marangoni forces [60], while the Ni was locally 'diluted' due to the uneven solute distribution. The DoA value in the P1B3 pair, mentioned in section 3.2.2, can serve as evidence of the occurrence of significant alloying during the solidification. Also, the calculated composition shown in figure 7(e) exemplifies that the principal element of the powder (Ni) distributes nonuniformly inside the deposited layer; the Fe as the principal element of baseplate spreads site-dependently, and its concentration decreases with distance to the bottom of the melt pool. Comparably, for the case depositing SS powder on the nickel-based alloy baseplate, the DoA for the clad layer of the P2B2 pair shows a 'majority' extent based on the calculation of the Ni element content (supplementary text B), suggesting that mutual re-alloying also occurred in the melts during solidification under the given parameter condition. Combined with figure S6, more Ni elements could be brought into the deposited layer, and a further part of the Fe gets diluted. In light of this, referring to results yielded by the pairs of homogeneous material, the hardness of the nickel/iron-based pair is weakened, while the resulting HV of the iron/nickel-based match shows an enhanced trend.

Interestingly, the hardness of the samples printed with the same or similar material combinations is almost consistent across the respective ZOI; however, the different material combinations present regional discontinuity, especially at the junction between the deposited layer and the dissimilar base material. From figure 7(f), the symbols within all the ZOIs of P1B1 and P1B2 (marked by blue and green) gather in a relatively concentrated interval of hardness value, while the symbols of P1B3 (marked by red) distribute more discretely, where the scatters within BZ correspond a less hardness value compared to those in EZ and PZ, with a deviation of approximately ∼60 $HV_{0.2}$. Concerning the combinations using powder SS316L (figure 7(g)), the red-marked symbols in all ZOIs distribute uniformly, which were sampled from the tracks printed with the same baseplate, whereas the hardness scatters for the case of the nickel-based alloys as the base material (marked by blue and green) vary with the ZOIs. The corresponding values at the interface are generally higher than those of the deposited layer (including EZ and PZ). Such regional discontinuity of hardness exhibited in samples using heterogeneous material combinations can be ascribed to the distinction of the alloy composition near the M-S junction resulting from solute redistribution in solidification. Because of the dissimil-

arity in the composition of the heterogeneous material pair, the solidified interface commonly crystallizes a distinct compositional transition zone or mutation zone concerning the principal elements, which can be demonstrated by the calculated element distribution (figures 7(e) and S6) and the measured chemical variation (figure S8). Such metallurgical weakness directly relates to differentiated mechanical properties and can adversely impact the bonding performance, which should be avoided marginally [19, 70].

4. Conclusions

In this study, incorporating experiments and the complementary simulation, the printability differences for using dissimilar material combinations of nickel- and iron-based alloys were investigated and interpreted from the macro- and microscale perspectives, respectively. The main contributions can be drawn as follows:

(1) Focusing on the DED process of single-track, the physical variation of melt pool propagation for respective material pairs was captured using high-speed imaging. The melt pools generated with nickel alloy powder and homogeneous base materials (P1B1 and P1B2) are morphologically larger than that deposited onto heterogeneous baseplate of iron-based alloy (P1B3), and their melt pool propagation is accompanied by relatively intense melt flow and more spatters. This is one of the macroscopic manifestations of the difference in printability of heterogeneous material combinations, where the surface tension and the viscosity of the liquid alloys played the essential factors. Also, due to the greater specific heat and thermal conductivity of the SS base material, the melt pool of depositing IN718 onto SS appears narrower and shallower than that of depositing IN718 onto nickel baseplates for a given parameter range.
(2) Microstructural diversity summarizes printability in the micro/internal aspect, characterized by differences in interfacial morphologies and grain growth. For the interfacial dissimilarity, a nearly sharp interface surrounding the melt pool in the single track can be generated due to the dissimilarity between the basic properties of powder and base materials (e.g. thermal conductivity, and solidification interval.). The interfacial morphologies of the bimetallic parts are associated with the deposition sequence of the concerned alloys, where a smooth transition interface is yielded for the P2/P1 combinations and an irregular transition for the inverse combinations, as the use of the materials of higher viscosity and density as the substrate is not conducive to the composition mixing within the melts. The grain feature discrepancy refers to the transformation within a single-track layer from columnar dendrites to equiaxed grains (P1B3), accompanied by grain size variation within a limited count of statistics (P1B3 is 45.5% larger than P1B1) as well as the cross-interface epitaxial growth for the P1/P2 bimetallic structures. These result from the synergistic effects of uneven alloy composition distribution and constitutional undercooling caused by solute redistribution during the specific solidification.
(3) As for the heterogeneous material combinations, in addition to the significant hardness variations at the interface, the hardness of the deposited layers also presents evident differentiation. Compared to the same material combinations, the microhardness within a deposited layer of the nickel-/iron-based pair is weakened, with an average decrease of 8.8%; while in turn, that of the iron-/nickel-based pair exhibits a 19.6% improvement for the deposited layer. The experimental results and the complementary simulation demonstrate that such heterogeneity can be interpreted by intermixing the principal elements of material pair and localized re-alloying in the solute during the solidification. The formation of the transition zone or the mutation region distinguished by the content of the principal element of the powder and the base material causes the discontinuity of microhardness between ZOIs.

This work follows the framework of 'material-process-property,' considering not merely the materials and process but also the forming quality and mechanical property, and aims to give more insight into the DED printability of bimetallic materials. Nickel- and iron-based alloys are selected for the comparative investigation; however, a thoughtless point exists herein, like the baseplates' microstructures were not uniformly controlled. In application-oriented bimetallic design and manufacturing, attention should be drawn to the microstructure and mechanical properties of the heterogeneous materials, especially for the inhomogeneity or discontinuity exhibited near the interface, which may potentially affect the application performance of the components. To further elucidate the complexity in solute redistribution during melt solidification and the effective control of the elemental mixing for tailoring more reliable structures, matching heterogeneous materials can be potential directions for future work.

Acknowledgments

This work was supported by the National Natural Science Foundation of China (51975112, 52375412), Fundamental Research Funds for Central Universities (N2203011).

Conflict of interest

The authors declare that they have no known competing financial interests or personal relationships that could have appeared to influence the work reported in this paper.

ORCID iDs

Jinsheng Ning https://orcid.org/0000-0002-0006-5993
Lida Zhu https://orcid.org/0000-0003-2777-202X
Zhichao Yang https://orcid.org/0000-0003-2269-3445
Amit Bandyopadhyay https://orcid.org/0000-0003-0992-5387

References

[1] Tan C L, Weng F, Sui S, Chew Y and Bi G J 2021 Progress and perspectives in laser additive manufacturing of key aeroengine materials *Int. J. Mach. Tools Manuf.* **170** 103804

[2] Bandyopadhyay A, Traxel K D, Lang M, Juhasz M, Eliaz N and Bose S 2022 Alloy design via additive manufacturing: advantages, challenges, applications and perspectives *Mater. Today* **52** 207–24

[3] Sui S, Chew Y, Weng F, Tan C L, Du Z L and Bi G J 2022 Study of the intrinsic mechanisms of nickel additive for grain refinement and strength enhancement of laser aided additively manufactured Ti–6Al–4V *Int. J. Extrem. Manuf.* **4** 035102

[4] Xue P S, Zhu L D, Xu P H, Ren Y, Xin B, Meng G R, Yang Z C and Liu Z 2021 Research on process optimization and microstructure of CrCoNi medium-entropy alloy formed by laser metal deposition *Opt. Laser Technol.* **142** 107167

[5] Bandyopadhyay A, Traxel K D and Bose S 2021 Nature-inspired materials and structures using 3D printing *Mater. Sci. Eng.* R **145** 100609

[6] Zuback J S, Palmer T A and DebRoy T 2019 Additive manufacturing of functionally graded transition joints between ferritic and austenitic alloys *J. Alloys Compd.* **770** 995–1003

[7] Feenstra D R, Banerjee R, Fraser H L, Huang A, Molotnikov A and Birbilis N 2021 Critical review of the state of the art in multi-material fabrication via directed energy deposition *Curr. Opin. Solid State Mater. Sci.* **25** 100924

[8] Wei C, Zhang Z Z, Cheng D X, Sun Z, Zhu M H and Li L 2021 An overview of laser-based multiple metallic material additive manufacturing: from macro- to micro-scales *Int. J. Extrem. Manuf.* **3** 012003

[9] Gu D D, Shi X Y, Poprawe R, Bourell D L, Setchi R and Zhu J H 2021 Material-structure-performance integrated laser-metal additive manufacturing *Science* **372** eabg1487

[10] Bandyopadhyay A and Heer B 2018 Additive manufacturing of multi-material structures *Mater. Sci. Eng.* R **129** 1–16

[11] Tammas-Williams S and Todd I 2017 Design for additive manufacturing with site-specific properties in metals and alloys *Scr. Mater.* **135** 105–10

[12] Chen W, Gu D D, Yang J K, Yang Q, Chen J and Shen X F 2022 Compressive mechanical properties and shape memory effect of NiTi gradient lattice structures fabricated by laser powder bed fusion *Int. J. Extrem. Manuf.* **4** 045002

[13] Svetlizky D, Das M, Zheng B L, Vyatskikh A L, Bose S, Bandyopadhyay A, Schoenung J M, Lavernia E J and Eliaz N 2021 Directed energy deposition (DED) additive manufacturing: physical characteristics, defects, challenges and applications *Mater. Today* **49** 271–95

[14] Panwisawas C, Tang Y T and Reed R C 2020 Metal 3D printing as a disruptive technology for superalloys *Nat. Commun.* **11** 2327

[15] Wang S H, Ning J S, Zhu L D, Yang Z C, Yan W T, Dun Y C, Xue P S, Xu P H, Bose S and Bandyopadhyay A 2022 Role of porosity defects in metal 3D printing: formation mechanisms, impacts on properties and mitigation strategies *Mater. Today* **59** 133–60

[16] DebRoy T, Mukherjee T, Milewski J O, Elmer J W, Ribic B, Blecher J J and Zhang W 2019 Scientific, technological and economic issues in metal printing and their solutions *Nat. Mater.* **18** 1026–32

[17] Afrouzian A, Groden C J, Field D P, Bose S and Bandyopadhyay A 2022 Additive manufacturing of Ti-Ni bimetallic structures *Mater. Des.* **215** 110461

[18] Bandyopadhyay A, Zhang Y N and Onuike B 2022 Additive manufacturing of bimetallic structures *Virtual Phys. Prototyp.* **17** 256–94

[19] Onuike B, Heer B and Bandyopadhyay A 2018 Additive manufacturing of Inconel 718—copper alloy bimetallic structure using laser engineered net shaping (LENS^{TM}) *Addit. Manuf.* **21** 133–40

[20] Sahasrabudhe H, Harrison R, Carpenter C and Bandyopadhyay A 2015 Stainless steel to titanium bimetallic structure using LENS^{TM} *Addit. Manuf.* **5** 1–8

[21] Li B Y, Han C J, Lim C W J and Zhou K 2022 Interface formation and deformation behaviors of an additively manufactured nickel-aluminum-bronze/15-5 PH multimaterial via laser-powder directed energy deposition *Mater. Sci. Eng.* A **829** 142101

[22] Zhang X C, Pan T, Chen Y T, Li L, Zhang Y L and Liou F 2021 Additive manufacturing of copper-stainless steel hybrid components using laser-aided directed energy deposition *J. Mater. Sci. Technol.* **80** 100–16

[23] Shinjo J and Panwisawas C 2022 Chemical species mixing during direct energy deposition of bimetallic systems using titanium and dissimilar refractory metals for repair and biomedical applications *Addit. Manuf.* **51** 102654

[24] Wang D *et al* 2022 Recent progress on additive manufacturing of multi-material structures with laser powder bed fusion *Virtual Phys. Prototyp.* **17** 329–65

[25] Lin X, Yue T M, Yang H O and Huang W D 2005 Laser rapid forming of SS316L/Rene88DT graded material *Mater. Sci. Eng.* A **391** 325–36

[26] Melzer D, Džugan J, Koukolíková M, Rzepa S and Vavřík J 2021 Structural integrity and mechanical properties of the functionally graded material based on 316L/IN718 processed by DED technology *Mater. Sci. Eng.* A **811** 141038

[27] Melzer D, Džugan J, Koukolíková M, Rzepa S, Dlouhý J, Brázda M and Bucki T 2022 Fracture characterisation of vertically build functionally graded 316L stainless steel with Inconel 718 deposited by directed energy deposition process *Virtual Phys. Prototyp.* **17** 821–40

[28] Zhang Y N and Bandyopadhyay A 2018 Direct fabrication of compositionally graded Ti-Al_2O_3 multi-material structures using laser engineered net shaping *Addit. Manuf.* **21** 104–11

[29] Ben-Artzy A, Reichardt A, Borgonia P J, Dillon R P, McEnerney B, Shapiro A A and Hosemann P 2021 Compositionally graded SS316 to C300 maraging steel using additive manufacturing *Mater. Des.* **201** 109500

[30] Tan C L, Liu Y C, Weng F, Ng F L, Su J L, Xu Z K, Ngai X D and Chew Y 2022 Additive manufacturing of voxelized heterostructured materials with hierarchical phases *Addit. Manuf.* **54** 102775

[31] Chen J, Yang Y Q, Song C H, Zhang M K, Wu S B and Wang D 2019 Interfacial microstructure and mechanical properties of 316L/CuSn10 multi-material bimetallic structure fabricated by selective laser melting *Mater. Sci. Eng.* A **752** 75–85

[32] Wei C, Gu H, Gu Y C, Liu L C, Huang Y H, Cheng D X, Li Z Q and Li L 2022 Abnormal interfacial bonding mechanisms of multi-material additive-manufactured tungsten–stainless steel sandwich structure *Int. J. Extrem. Manuf.* **4** 025002

[33] Zhang Y N and Bandyopadhyay A 2021 Influence of compositionally graded interface on microstructure and compressive deformation of 316L stainless steel to Al12Si aluminum alloy bimetallic structures *ACS Appl. Mater. Interfaces* **13** 9174–85

[34] Wei C *et al* 2022 Cu10Sn to Ti6Al4V bonding mechanisms in laser-based powder bed fusion multiple material additive

manufacturing with different build strategies *Addit. Manuf.* **51** 102588
[35] Li W, Karnati S, Kriewall C, Liou F, Newkirk J, Brown Taminger K M and Seufzer W J 2017 Fabrication and characterization of a functionally graded material from Ti-6Al-4V to SS316 by laser metal deposition *Addit. Manuf.* **14** 95–104
[36] Shi Q M, Zhong G Y, Sun Y, Politis C and Yang S F 2021 Effects of laser melting+remelting on interfacial macrosegregation and resulting microstructure and microhardness of laser additive manufactured H13/IN625 bimetals *J. Manuf. Process.* **71** 345–55
[37] Zhang W X, Hou W Y, Deike L and Arnold C 2022 Understanding the Rayleigh instability in humping phenomenon during laser powder bed fusion process *Int. J. Extrem. Manuf.* **4** 015201
[38] Chen Y W, Zhang X, Li M M, Xu R Q, Zhao C and Sun T 2020 Laser powder bed fusion of Inconel 718 on 316 stainless steel *Addit. Manuf.* **36** 101500
[39] Yang Z C, Wang S H, Zhu L D, Ning J S, Xin B, Dun Y C and Yan W T 2022 Manipulating molten pool dynamics during metal 3D printing by ultrasound *Appl. Phys. Rev.* **9** 021416
[40] Hofmann D C, Roberts S, Otis R, Kolodziejska J, Dillon R P, Suh J O, Shapiro A A, Liu Z K and Borgonia J P 2014 Developing gradient metal alloys through radial deposition additive manufacturing *Sci. Rep.* **4** 5357
[41] Tumkur T U *et al* 2021 Nondiffractive beam shaping for enhanced optothermal control in metal additive manufacturing *Sci. Adv.* **7** eabg9358
[42] Scipioni Bertoli U, Guss G, Wu S, Matthews M J and Schoenung J M 2017 In-situ characterization of laser-powder interaction and cooling rates through high-speed imaging of powder bed fusion additive manufacturing *Mater. Des.* **135** 385–96
[43] Siva Prasad H, Brueckner F and Kaplan A F H 2020 Powder incorporation and spatter formation in high deposition rate blown powder directed energy deposition *Addit. Manuf.* **35** 101413
[44] Ebrahimi A, Kleijn C R and Richardson I M 2021 Numerical study of molten metal melt pool behaviour during conduction-mode laser spot melting *J. Appl. Phys.* **54** 105304
[45] Mumtaz K A and Hopkinson N 2010 Selective laser melting of thin wall parts using pulse shaping *J. Mater. Process. Technol.* **210** 279–87
[46] Sikandar Iquebal A, Yadav A, Botcha B, Krishna Gorthi R and Bukkapatnam S 2022 Tracking and quantifying spatter characteristics in a laser directed energy deposition process using Kalman filter *Manuf. Lett.* **33** 692–700
[47] Criales L E, Arısoy Y M, Lane B, Moylan S, Donmez A and Özel T 2017 Laser powder bed fusion of nickel alloy 625: experimental investigations of effects of process parameters on melt pool size and shape with spatter analysis *Int. J. Mach. Tools Manuf.* **121** 22–36
[48] Coen V, Goossens L and van Hooreweder B 2022 Methodology and experimental validation of analytical melt pool models for laser powder bed fusion *J. Mater. Process. Technol.* **304** 117547
[49] Zhao C, Shi B, Chen S L, Du D, Sun T, Simonds B J, Fezzaa K and Rollett A D 2022 Laser melting modes in metal powder bed fusion additive manufacturing *Rev. Mod. Phys.* **94** 045002
[50] Wang J H, Han F Z, Chen S F and Ying W S 2019 A novel model of laser energy attenuation by powder particles for laser solid forming *Int. J. Mach. Tools Manuf.* **145** 103440
[51] Haley J C, Schoenung J M and Lavernia E J 2018 Observations of particle-melt pool impact events in directed energy deposition *Addit. Manuf.* **22** 368–74
[52] Chen Y H *et al* 2021 Correlative synchrotron x-ray imaging and diffraction of directed energy deposition additive manufacturing *Acta Mater.* **209** 116777
[53] Khorasani M, Ghasemi A, Leary M, Cordova L, Sharabian E, Farabi E, Gibson I, Brandt M and Rolfe B 2022 A comprehensive study on meltpool depth in laser-based powder bed fusion of Inconel 718 *Int. J. Adv. Manuf. Technol.* **120** 2345–62
[54] Shamsaei N, Yadollahi A, Bian L and Thompson S M 2015 An overview of direct laser deposition for additive manufacturing; part II: mechanical behavior, process parameter optimization and control *Addit. Manuf.* **8** 12–35
[55] Ghanavati R, Naffakh-Moosavy H, Moradi M and Eshraghi M 2022 Printability and microstructure of directed energy deposited SS316l-IN718 multi-material: numerical modeling and experimental analysis *Sci. Rep.* **12** 16600
[56] Galbusera F, Demir A G, Platl J, Turk C, Schnitzer R and Previtali B 2022 Processability and cracking behaviour of novel high-alloyed tool steels processed by laser powder bed fusion *J. Mater. Process. Technol.* **302** 117435
[57] Wang A *et al* 2023 Effects of processing parameters on pore defects in blue laser directed energy deposition of aluminum by in and ex situ observation *J. Mater. Process. Technol.* **319** 118068
[58] Hinojos A, Mireles J, Reichardt A, Frigola P, Hosemann P, Murr L E and Wicker R B 2016 Joining of Inconel 718 and 316 stainless steel using electron beam melting additive manufacturing technology *Mater. Des.* **94** 17–27
[59] Yang Z C, Zhu L D, Wang S H, Ning J S, Dun Y C, Meng G R, Xue P S, Xu P H and Xin B 2021 Effects of ultrasound on multilayer forming mechanism of Inconel 718 in directed energy deposition *Addit. Manuf.* **48** 102462
[60] Yao L M, Huang S, Ramamurty U and Xiao Z M 2021 On the formation of "Fish-scale" morphology with curved grain interfacial microstructures during selective laser melting of dissimilar alloys *Acta Mater.* **220** 117331
[61] Ghanavati R, Naffakh-Moosavy H and Moradi M 2021 Additive manufacturing of thin-walled SS316L-IN718 functionally graded materials by direct laser metal deposition *J. Mater. Res. Technol.* **15** 2673–85
[62] Chen N N, Khan H A, Wan Z X, Lippert J, Sun H, Shang S L, Liu Z K and Li J J 2020 Microstructural characteristics and crack formation in additively manufactured bimetal material of 316L stainless steel and Inconel 625 *Addit. Manuf.* **32** 101037
[63] Xiao Y H, Wan Z X, Liu P W, Wang Z, Li J J and Chen L 2022 Quantitative simulations of grain nucleation and growth at additively manufactured bimetallic interfaces of SS316L and IN625 *J. Mater. Process. Technol.* **302** 117506
[64] Mukherjee T, DebRoy T, Lienert T J, Maloy S A and Hosemann P 2021 Spatial and temporal variation of hardness of a printed steel part *Acta Mater.* **209** 116775
[65] Dinda G P, Dasgupta A K and Mazumder J 2021 Texture control during laser deposition of nickel-based superalloy *Scr. Mater.* **67** 503–6
[66] Tan Z E, Pang J H L, Kaminski J and Pepin H 2019 Characterisation of porosity, density, and microstructure of directed energy deposited stainless steel AISI 316L *Addit. Manuf.* **25** 286–96
[67] Wolff S J, Gan Z T, Lin S, Bennett J L, Yan W T, Hyatt G, Ehmann K F, Wagner G J, Liu W K and Cao J 2019 Experimentally validated predictions of thermal history and microhardness in laser-deposited Inconel 718 on carbon steel *Addit. Manuf.* **27** 540–51

[68] Zhang L, Wen M, Imade M, Fukuyama S and Yokogawa K 2008 Effect of nickel equivalent on hydrogen gas embrittlement of austenitic stainless steels based on type 316 at low temperatures *Acta Mater.* **56** 3414–21
[69] Zuback J S and DebRoy T 2018 The hardness of additively manufactured alloys *Materials* **11** 2070
[70] Adomako N K, Lewandowski J J, Arkhurst B M, Choi H, Chang H J and Kim J H 2022 Microstructures and mechanical properties of multi-layered materials composed of Ti-6Al-4V, vanadium, and 17–4PH stainless steel produced by directed energy deposition *Addit. Manuf.* **59** 103174